Interface extension is a continuum property suggesting a linkage between AP contractile and DV lengthening processes

Timothy E. Vanderleest[a], Yi Xie[b], Celia Smits[b], J. Todd Blankenship[b,*], and Dinah Loerke[a,*]
[a]Department of Physics and Astronomy and [b]Department of Biological Sciences, University of Denver, Denver, CO 80208

ABSTRACT **In the early *Drosophila* embryo, the elongation of the anterior-posterior (AP) body axis is driven by cell intercalation in the germband epithelium. Neighboring cells intercalate through the contraction of AP interfaces (between AP neighbors) into higher-order vertices, which then resolve through the extension of new dorsal-ventral (DV) interfaces (between DV neighbors). Although interface contraction has been extensively studied, less is known about how new interfaces are established. Here we show that DV interface elongation behaviors initiate at the same time as AP contractions, and that DV interfaces which are newly created from resolution of higher-order vertices do not appear to possess a unique 'identity;' instead, all horizontal interfaces undergo lengthening, elongating through ratchet-like sliding behaviors analogous to those found in AP interfaces. Cortical F-actin networks are essential for high area oscillation amplitudes required for effective ratcheting. Our results suggest that, contrary to canonical models, the elongation of new DV interfaces is not produced by a mechanistically separate process. Instead, medial myosin populations drive oscillating radial forces in the cells to generate transient force asymmetries at all tricellular vertices, which—combined with planar polarized stabilization—produce directional ratcheted sliding to generate both AP interface contraction and DV interface elongation.**

Monitoring Editor
Alpha Yap
University of Queensland

Received: Jul 14, 2021
Revised: Sep 7, 2022
Accepted: Sep 14, 2022

INTRODUCTION

Cell intercalation is a fundamental process underlying tissue reshaping in morphogenesis (Irvine and Wieschaus, 1994; Keller *et al.*, 2000, 2002; Wallingford *et al.*, 2002; Nikolaidou and Barrett, 2005; Solnica-Krezel, 2005). One of the morphogenetic processes driven by cell intercalation is the elongation of the germ band in the early *Drosophila* embryo (Guillot and Lecuit, 2013; Loerke and Blankenship, 2020), where systematic cell intercalation produces convergent extension (convergence of the tissue in the dorsal-ventral (DV) dimension and extension in the anterior-posterior (AP) dimension), resulting in elongation of the body axis (Irvine and Wieschaus, 1994; Bertet *et al.*, 2004; Zallen and Wieschaus, 2004). In the germband epithelium, cell intercalation happens through directional swapping of cell–cell contacts, where cell contacts between AP neighboring cells contract into a multicellular vertex, followed by the resolution of this higher-order vertex into a new perpendicular cell contact between DV neighbors.

In the following, we use a nomenclature where AP borders (which we call AP interfaces) are defined as contacts between AP neighboring cells, and DV interfaces are contacts between DV neighboring cells (Zallen and Wieschaus, 2004). We will often refer to these as "vertical" or "horizontal" interfaces, respectively, following the standard practice of orienting images with the AP body axis into the horizontal direction. In addition, we use a nomenclature (Bertet *et al.*, 2004; Vanderleest *et al.*, 2018) in which the contracting vertical interface is called a "Type 1 configuration" (or T1 interface), the resulting higher-order (four-way) vertex is called a "Type 2 configuration" (or T2 vertex), and its subsequent resolution into a horizontal interface a "Type 3' configuration" (or T3 interface). We use the term "T3 interface" here specifically to identify horizontal interfaces

This article was published online ahead of print in MBoC in Press (http://www.molbiolcell.org/cgi/doi/10.1091/mbc.E21-07-0352) on September 21, 2022.

*Address correspondence to: Dinah Loerke (dinah.loerke@du.edu); Todd Blankenship (todd.blankenship@du.edu).

Abbreviations used: AP, anterior-posterior; DV, dorsal-ventral; GBE, germ band extension; GFP, green fluorescent protein; KS, Kolmogorov-Smirnov; MSD, mean squared displacement; PEH, pre-existing horizontal; ROI, region of interest; SD, standard deviation; SF, shape factor; SEM, standard error of the mean.

that are newly generated from the resolution of T2 vertices to distinguish them from any pre-existing horizontal interfaces that were already present at the beginning on germ band extension. However, as a point of clarification, our terminology is not to be confused with the more common naming practice (originating from soft matter physics) where the entire topological transition between the contracting vertical to the elongating horizontal interface is considered a "T1 process/transition" and where the terms "T2" and "T3" would refer to completely distinct topological processes.

The necessary directional preference (and thus symmetry breaking) of the intercalation process is regulated through a system of planar polarity within the tissue, with anisotropic distributions of actomyosin and adhesion molecules at the level of the cell (Irvine and Wieschaus, 1994; Bertet *et al.,* 2004; Zallen and Wieschaus, 2004; Blankenship *et al.,* 2006; Simões *et al.,* 2010; Sawyer *et al.,* 2011; Levayer and Lecuit, 2013). While much of the effort of research into this process has focused on the contraction of vertical interfaces, and particularly into the associated planar polarized actomyosin recruitment (Rauzi *et al.,* 2008; Fernandez-Gonzalez *et al.,* 2009; Simões *et al.,* 2010, 2014; Munjal *et al.,* 2015; Garcia De Las Bayonas *et al.,* 2019), the subsequent resolution of new contacts is less well understood.

Notably, while horizontal interface elongation behavior is planar polarized, unlike vertical interfaces they lack a clearly visible molecular correlate, such as the preferential localization of a specific molecule to these newly formed horizontal interfaces (Blankenship *et al.,* 2006; Simoes *et al.,* 2010). Many initial studies in the field assumed implicitly or explicitly that the growth of new junctions could be a passive process in which mechanical stresses that were "loaded" by the AP interface contraction are subsequently relaxed. Indeed, in computational models of intercalation, this assumption is sufficient to drive T3 interface elongation (Glazier and Graner, 1993; Farhadifar *et al.,* 2007; Käfer *et al.,* 2007; Rauzi *et al.,* 2008; Hilgenfeldt *et al.,* 2008; Aigouy *et al.,* 2010). In other systems, it has been shown that active (as opposed to passive relaxation) mechanisms can play a role in new interface elongation, including a role for mechanical tension in the mouse embryonic ectoderm during limb bud elongation (Lau *et al.,* 2015) and an active reduction of line tension (through prevention of myosin II enrichment) at new junctions in the *Drosophila* dorsal thorax (Bardet *et al.,* 2013). In the fly germband, the first evidence that active mechanisms play a role during the growth of new interfaces has come from work suggesting the existence of a medial pulling force in neighboring AP cells (Collinet *et al.,* 2015), as well as a reduced line tension at T3 interfaces (Yu and Fernandez-Gonzalez, 2016). However, a systematic analysis of cell shape parameters, and whether and how they change as cells form and then resolve higher-order vertex configurations, has not been performed.

Filamentous actin (F-actin) and nonmuscle myosin II are key proteins known to be directly involved in vertical interface contraction in GBE. Myosin II is planar polarized and becomes enriched at vertical interfaces, where it is canonically thought to contract the interface via increased line tension (Bertet *et al.,* 2004; Zallen and Wieschaus, 2004; Blankenship *et al.,* 2006; Rauzi *et al.,* 2008; Fernandez-Gonzalez *et al.,* 2009). Cortical F-actin networks also enforce cell rigidity, and the turnover of these networks correlates with the dissipative relaxation of elastic forces at the cell surface (Clément *et al.,* 2017). Recently, however, we have proposed that vertical interface contractions operate through a system of ratcheted tricellular vertex sliding movements directed by cell area oscillations and vertex-based myosin II populations (Vanderleest *et al.,* 2018). It is also notable that, in contrast to the canonical focus on interface-parallel tension forces described above, recent studies on T3 interface elongation have also suggested the possibility of radially directed forces during new interface extension (Collinet *et al.,* 2015; Yu and Fernandez-Gonzalez, 2016). There is, therefore, a great deal of interest in whether the canonical models of T1 transitions in intercalation should be reframed in terms of radial and medial force generation events that are coupled with oscillations in cell areas. In this study, we have investigated where active, local elongation forces come from and when they are initialized. Surprisingly, we found that horizontal interface elongation dynamics begin in the tissue at the same time as vertical contraction dynamics, and that they operate on *any interface that is oriented along the AP axis*. Thus pre-existing horizontal interfaces grow at comparable rates as new T3 interfaces, demonstrating that the ability to grow horizontally is not a molecular privilege that T3 interfaces gain from their history of new initiation. In addition, vertical interface contraction and horizontal interface elongation demonstrate a striking symmetry of their behaviors, occurring as ratcheted steps in a framework of cell area oscillations. Thus we propose that vertical contraction and T3 elongation, rather than arising from molecularly and/or mechanically distinct processes, originate from the same continuum of radial forces and spatial ratchet asymmetries.

RESULTS

The rate of horizontal T3 interface elongation is similar to vertical interface contraction

As a first approach to study how new interfaces initiate and grow, we wanted to systematically explore the rates by which interfaces contract and grow in an automatically determined manner. We segmented and tracked GBE cells during cell intercalation in the early embryo and measured interface dynamics including changes in interface length with a temporal resolution of 1 s in control embryos (Figure 1, A and A′).

To examine the relationships between vertical T1 interface contractions and horizontal T3 interface elongations, as well as how cells transition between these behaviors, we first directly compared T1 contraction and T3 elongation rates. To this end, we aligned the original time courses of the transitions (Figure 1A′) to the time points of the higher-order vertex (which we will call the "T2 time point" in the following) and averaged the aligned length time courses (Figure 1B). By convention, we assign negative lengths to new horizontal interfaces in order to distinguish them from vertical interfaces, and we constrained the analysis to those transition time courses where the interfaces were continuously visible over the entire specified time period (specifically, $n = 389$ time courses where the interface is visible in the field of view continuously from 5 min before to 5 min after the T2 time point. Interestingly, the results indicate that contractile behaviors speed up (i.e., steeper slopes in Figure 1B) as interfaces get closer to the T2 time point. Additionally, there is a striking symmetry around the T2 time point as interfaces transition between contractile and expansion behaviors (Figure 1B). To examine these dynamics in more detail, we calculated the associated time-resolved progression rate (Figure 1B′), which is the time-resolved slope (calculated in a 30-s time window) of the average length time course in Figure 1B. Consistent with the length time courses, this time-resolved rate shows a distinct peak centered around T2, with the center of mass of the maximum shifted toward the T1 phase. The prepeak "baseline" progression rate in T1 was slightly higher than the postpeak baseline in T3 (approximately 0.45 μm/min in T1 vs. 0.35 μm/min in T3), with the peak rates close to the T2 time point reaching 0.8 μm/min. These similarities in dynamics between T1s and T3s were intriguing, which prompted us to look

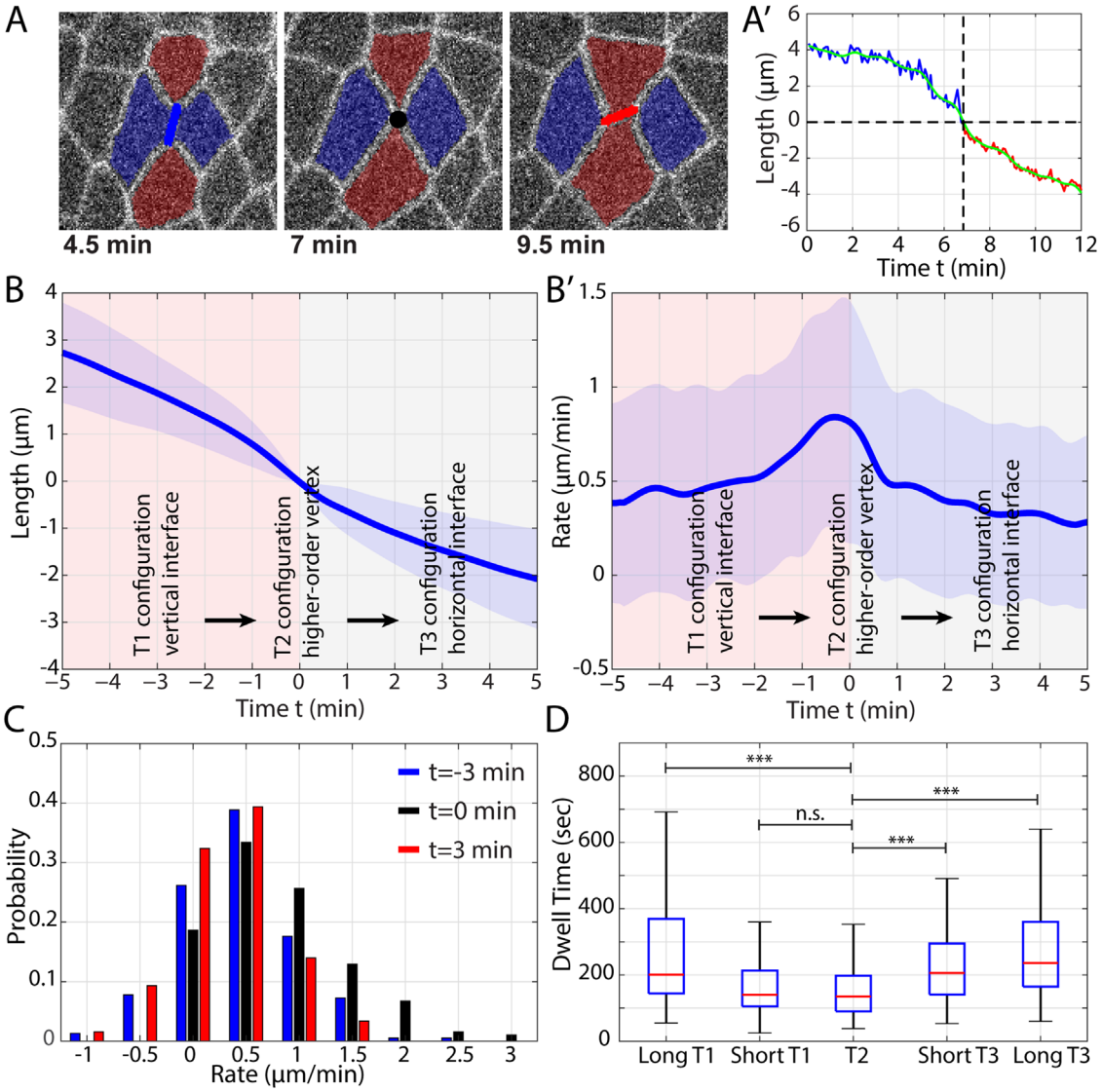

FIGURE 1: T3 interface elongation has similar rates to T1 interface contraction, and there is no evidence for significant T2 dwell times. (A) Snapshots of a T1-T2-T3 transition with a color overlay of the T1 interface (blue), T2 vertex (black), and T3 interface (red). (A′) Length trace of the transition in (A) using the same color scheme. The T3 interface length is assigned a negative value. (B) Average interface length and (B′) interface length change rate for transitions that were tracked continuously for 5 min pre- and post-T2 ($n = 389$ transitions, $k = 21$ embryos) aligned to the T2 configuration time point. Shaded confidence interval represents SD in both B and B′. (C) Probability density of the rates at $t = –3$ min (in T1), $t = 0$ min (at T2), and $t = +3$ min (in T3) for the data shown in (B-B′). (D) Box plot (see *Materials and Methods*) of dwell time (in seconds) spent inside a 1.6-μm-length interval, with the interval centered at 3.2 μm (Long T1), 1.6 μm (Short T1), 0 μm (T2), –1.6 μm (Short T3), and –3.2 μm (Long T3); $n = 182$ transitions; n.s. indicates $P \geq 0.05$ and *** indicates $P < 0.001$ results from two-sample Kolmogorov–Smirnov test.

more closely at the dynamics that occur as these interfaces undergo this rapid transition in their behaviors.

There is no evidence for significant T2 dwell times

In addition to the symmetry between T1 and T3, the time course analysis also revealed an increase in the length change rate—faster T1 contractions and T3 elongations—centered around the T2 time point. This increased rate during the transition through the T2 time point is the opposite of what would be expected if significant T2 dwell times existed and argues against any systematic stalling at the T2 configuration. The relatively smooth transition between T1 contractile behaviors and T3 extension dynamics is also readily apparent in representative movies of T1-T3 transitions (Supplemental Video S1). However, we wanted to test the possibility that the average rates shown in Figure 1B′ could represent the conflation of heterogeneous behaviors, for example, the superposition of one interface population that stalls in the T2 configuration with a second actively contracting/elongating population. To examine this hypothesis, we measured the distribution of total contraction/elongation rates for these interfaces at the $t = –3$ min time point (during prepeak baseline T1), at $t = +3$ min (during postpeak baseline T3), and at the T2 reference time point $t = 0$ (Figure 1C). All three rate distributions appear to be largely monomodal distributions, with the means of the distributions consistent with the values from Figure 1B′. These data argue against any substantial stalled subpopulation of T2 configurations. Finally, in order to avoid any confounding

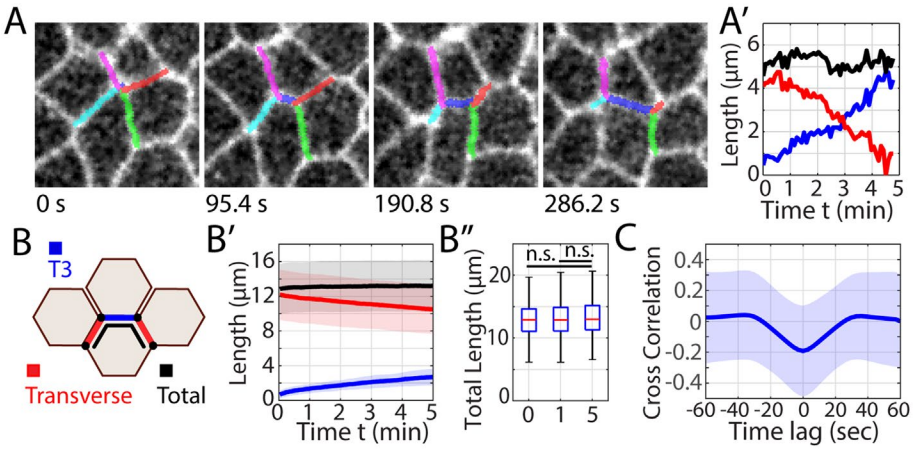

FIGURE 2: New interface elongation occurs through vertex sliding. (A) Snapshots of an elongating T3 interface (blue) and its four associated transverse interfaces highlighted in different colors, starting from the T2 configuration at $t = 0$s to $t = 286$s later. (A′) Length traces of the T3 interface (blue), one transverse interface (red), and the sum of the two lengths (black) for the example shown in A. (B) Diagram of the T3 (blue), two transverse interfaces (red), and the sum of the three (black line). (B′) Average length trace of T3s aligned to T2 (blue), the sum of the two transverse interfaces (red), and the total length of the three interfaces (black) over 5 min from the T2 time point ($n = 528$). (B″) Box plot (see *Materials and Methods*) of the three-interface sum at $t = 0$, $t = 1$, and $t = 5$ min; n.s. indicates $P \geq 0.05$ from a two-sample Kolmogorov–Smirnov test. (C) Average temporal cross-correlation between the rate of T3 length change with the rate of length change for a transverse interface pair ($n = 1060$). Shaded confidence intervals represent SD in (B′, C). All data above from $k = 17$ embryos.

factors that could be introduced by very short interfaces (lengths less than 1–2 camera pixels that could introduce noise in the segmentation results; see *Materials and Methods*), we used an orthogonal analytical approach. In this analysis, the time that interfaces spent in five equal-sized length bins was measured during the transition from T1 to T3 (Figure 1D). Interestingly, and consistent with our above analysis, these results demonstrate that less time is spent in the T2 bin (ranging from 0.8 to –0.8 μm length) than in the long T1 and T3 length bins. Short T1 dwell times were not significantly greater, which is consistent with T1 transition rates peaking just before T2. These data indicate that the transition speed (rate of length change) increases in the time window around the T2 configuration. In total, the similarity of T1 and T3 time courses, as well as the absence of T2 dwell times, suggests that there could be an unrevealed continuity to the mechanism that drives T1 contraction and T3 elongation. This also suggests that there is likely no functional intermediate step in the transition from T1 to T3 topologies.

T3 interface elongation occurs via a vertex sliding mechanism

We previously identified a new mechanism of interface contraction that involves the sliding of tricellular vertices, in which contractions of the T1 interfaces are immediately compensated by similar magnitude elongations of the associated transverse interfaces (Vanderleest *et al.*, 2018). Spurred by the symmetry of the T1-T3 transition shown above, we wanted to test whether the mechanism of T3 elongation was similar to T1 contraction, so we repeated the sliding analysis on T3 interfaces. We found that, like T1 interfaces, elongation of T3 interfaces could generally be seen to show a compensation in the length of the four associated transverse interfaces. For example, contractions of the cyan and red transverse interfaces (Figure 2A) mirror the elongation behaviors of the T3 interface, and the sum total of the transverse lengths and T3 lengths is approximately constant as the new T3 interface grows in length (Figure 2A′; Supplemental Video S2). This could also be shown systematically ($n = 528$ T3 interfaces), as we found that the sum of the lengths of the T3 with the two transverse junctions on the same DV cell led to fairly equal compensation between T3 elongation and transverse interface contractions (Figure 2B). Over 5 min of T3 growth, the length sum of the three interfaces only increased by 0.4 μm (Figure 2, B′ and B″), while the measured transverse and T3 interface lengths showed nearly identical reciprocal behaviors. As an additional test of how changes in the T3 length temporally correlated with changes in the transverse junctions, we performed a cross-correlation of the T3 length gradient with each of the four transverse junction length gradients to determine if there was immediate compensation as the T3 interface expanded. On average, the T3 length changes were anticorrelated with transverse junction length changes with no temporal lag (Figure 2C). These results show that, similarly to T1 interfaces, T3 elongations happen in a sliding manner where transverse interfaces instantaneously shorten through vertex displacements.

T3s elongation is not driven primarily by elasticity of cell shapes

One potential mechanism for driving the elongation of newly created T3 interfaces is the relaxation of elastic tension forces, which conceptually try to minimize the surface per volume of the cell. In the two-dimensional cross-section image, this corresponds to a minimization of perimeter per area, which drives a preference for the most "rounded" cell shapes and corresponding hexagonal topologies. During (actively driven) T1 interface contraction, participating cells lose a minimum of one side and cell topologies becomes increasingly disordered (Figure 3, A-A′). Thus from the perspective of elastic energies, the elongation of new T3 interfaces could be energetically favorable because they achieve the addition of a new side to two cells, allowing these to relax back into a more "rounded" shape. We wanted to examine this possibility more closely so measured a cell shape factor (SF) for intercalating cells (defined as $Perimeter^2/(4\pi * Area)$, which equals 1 for a circle and increases for more elongated or irregular shapes) as a function of time. When we average this metric over all visible cells of the germ band and synchronize it with respect to the start of cell intercalation (Figure 3, A and A′), we found that the shape metric starts to increase slightly before the onset of GBE (likely due to cells being slightly stretched out during ventral furrow formation). The SF then continues to increase significantly for the first 12–13 min of GBE, after which it plateaus for the next 20 min. Importantly, a significant decrease of the SF (i.e., restoration of cell roundedness) was not observed in the germband epithelium during the time period associated with robust T3 interface elongation. Since we were interested in whether T3 elongation specifically contributes to cell shape relaxation, we repeated this analysis at the level of cells participating in T1-T3 transitions, where we aligned their SF time courses with respect to the T2 time point (Figure 3, B-B′). In keeping with our expectations based on the cell geometries during T1 interface

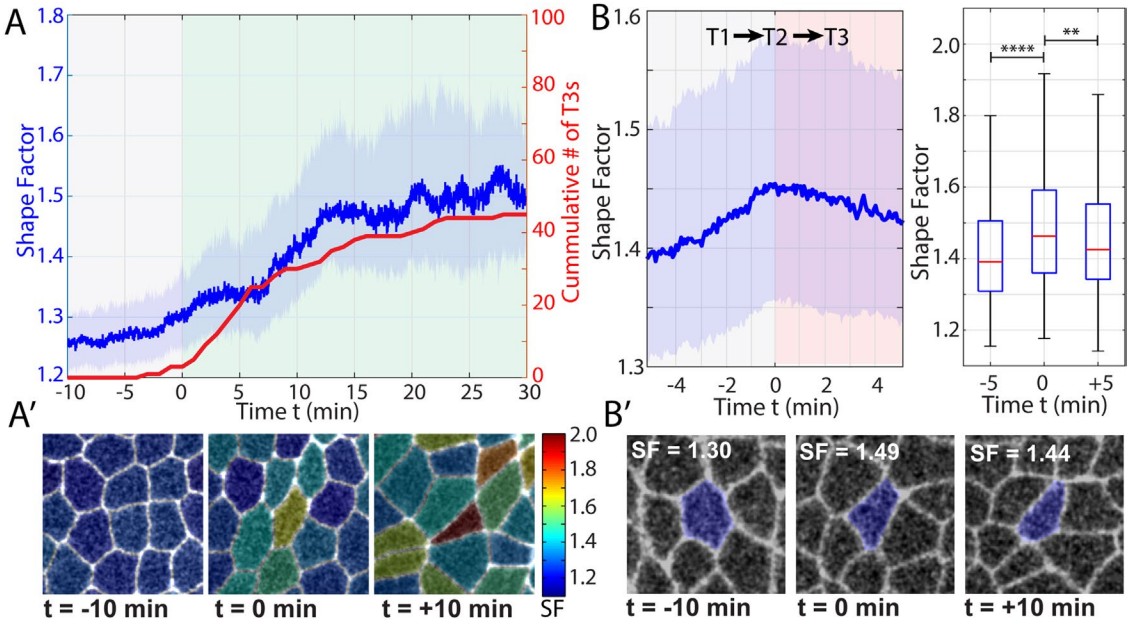

FIGURE 3: T3 interface elongation is not driven by an elastic relaxation of cell shapes. (A) Median cell SF (blue) with respect to the start of GBE ($n = 1210$ cells, $k = 3$ embryos) and cumulative sum of the number of new T3 interfaces (red). Shaded confidence interval represents interquartile range. (A′) Snapshots of cells colored by their SF for time points 10 min before, at the start of, and 10 min into GBE. (B) Median cell SF during transition, aligned to the T2 configuration time point ($n = 820$ cells, $k = 16$ embryos; for each transition, all four participating cells were included for the full time window). Shaded confidence interval represents interquartile range. Box plot of cell SF from same data set at three time points; ** indicates $P \leq 0.01$ and **** indicates $P \leq 0.0001$, two-sample Kolmogorov–Smirnov test. (B′) SF (SF) for an individual cell (highlighted in blue) that is in the process of contracting its right vertical interface, measured 10 min before (left), at (middle), and 10 min after (right) T2 configuration.

contraction, we found that cell SFs increase up to the T2 time point and then plateau before beginning to decrease very slightly. This finding suggests that: 1) the SF increase observed in Figure 3A is indeed driven at least in part by T1 interface contraction and the corresponding changes in cell sidedness, but that 2) the elongation of new T3 interfaces does not substantially restore the roundness of the cells. Thus these results together suggest that passive elastic, shape-restoring forces likely only play a small role in driving T3 interface elongation, but that other, active processes will be major drivers in causing interface lengthening. These results are also consistent with previous studies arguing for myosin II- and PMG-dependent processes in assisting interface elongation (Collinet *et al.*, 2015; Yu and Fernandez-Gonzalez, 2016).

All GBE interfaces oriented along the A-P axis are subject to elongation forces

While examining the onset of planar polarized behaviors of T3 interfaces, we wanted to know *when* the forces that cause interface lengthening are initiated. Furthermore, given the similarity in rates between T1 and T3 processes, we decided to examine if there was a similar temporal onset of the contractile and interface extending rates. However, since bona fide T3 interfaces are created through T1 contraction into a T2 configuration and its subsequent resolution, most T3 interfaces will not appear until some minutes after T1 contraction has been initiated. Thus in order to examine elongation behavior in the early stages of GBE, we first asked if "pre-existing" horizontal interfaces (i.e., horizontal interfaces aligned along the AP axis that are *not* newly created through T1-T3 transition but that are already present prior to the start of germ-band extension; see *Materials and Methods*) demonstrate any dynamic behaviors. Intriguingly, we found that these pre-existing interfaces also start to elongate directly at the onset of GBE, well before any T3 horizontal interfaces are present (Figure 4, A and A′). Additionally, a comparison with the onset of T3 elongation rates demonstrated that new T3 horizontal interfaces already appear "primed" to extend, with the earliest observable T3 interfaces possessing the highest elongation rates (Figure 4B). This would be consistent with the idea that the cellular forces that drive T3 elongation already exist prior to the generation of new T3 interfaces.

Pre-existing horizontal interfaces have similar extension dynamics to T3 interfaces

These findings raised the question as to whether there is any difference in the elongation mechanisms between bona fide T3 horizontal interfaces (which newly emerge from a T2 configuration) and "pre-existing" horizontal interfaces (referred to in the following as PEHs) which are oriented in the same direction as the A-P axis (Figure 4A). To answer this question, we compared the rates of progression in PEHs as well as T1 and T3 interfaces as a function of developmental time (Figure 4C). Remarkably, we found that at the very start of GBE, the rate of contractile behaviors in T1 interfaces and elongation behaviors in PEH interfaces initiates with very similar dynamics and magnitudes (Figure 4C and Supplemental Figure S4E). This suggests that the forces driving the contraction of vertical interfaces oriented along the D-V axis are present at the same time as those that drive horizontal interface elongation. The number of newly formed T3 interfaces became sufficient for reliable statistics (Figure 4C′) after approximately 7.5 min of GBE at approximately the same time at which elongation speed peaks. Going forward from this time point, T3 interfaces had similar elongation rates to PEH interfaces, and both populations saw a similar decreasing trend after about 12 min into GBE (Figure 4C).

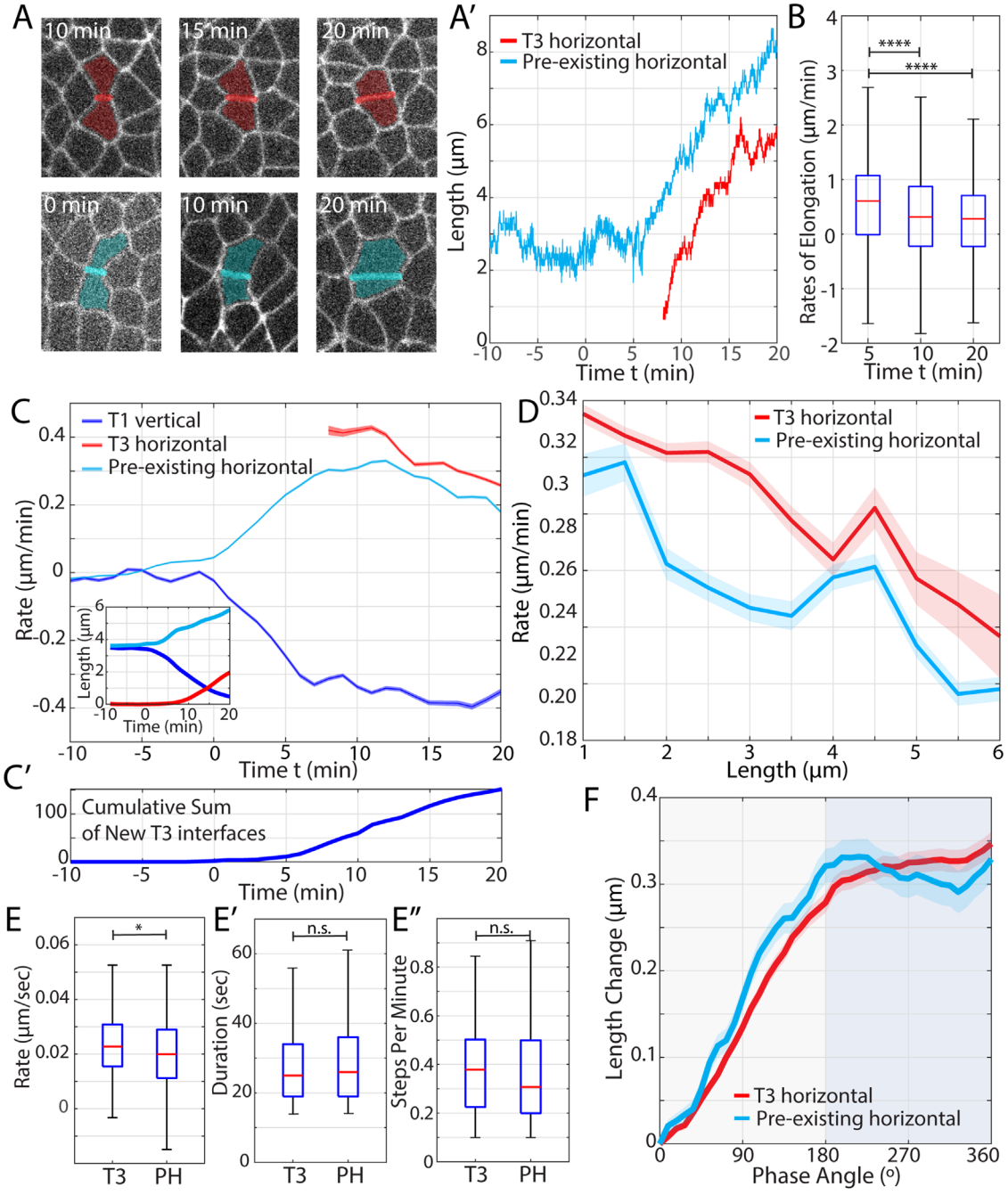

FIGURE 4: New T3 horizontal interfaces have similar dynamics to pre-existing horizontal interfaces. (A) Snapshots of a T3 horizontal interface (top row, red) and a pre-existing horizontal interface (bottom row, cyan) shown at different time points with respect to the start of GBE. (A′) Length traces of the T3 horizontal (red) and pre-existing horizontal (cyan) interfaces shown in A. (B) Elongation rates of T3 interfaces, measured during the 1-min time interval centered at 5, 10, or 20 min with respect to the start of GBE (minimum $n = 2632$ time points for each interval). (C) Time-resolved mean rates of length change for T1 interfaces (blue), T3 interfaces (red), and pre-existing horizontal interfaces (cyan). (C′) Cumulative sum of the number of new T3 interfaces over developmental time. (D) Length-resolved rates of T3 horizontal interfaces ($n = 1127$ interfaces) and pre-existing horizontal interfaces ($n = 1266$). (E-E″) Box plot of detected step rates, durations, and step frequency for T3 horizontal and pre-existing horizontal (PH) interfaces ($n = 206$ steps from 97 unique T3 interfaces; $n = 266$ steps from 100 unique PH interfaces). (F) Mean length changes during cell area oscillation cycles for T3 horizontal (red, $n = 2490$ cycles) and pre-existing horizontal interfaces (cyan, $n = 1,855$ cycles). All panels: shaded confidence interval represent SEM; n.s. indicates $P \geq 0.05$, * indicates $P < 0.05$, and **** indicates $P < 0.0001$, two-sample Kolmogorov–Smirnov test. All data above from $k = 21$ embryos.

While the dynamics of the elongation rates are strikingly similar between T3s and pre-existing horizontal interfaces, Figure 4C still shows a small but systematic difference in the magnitude, with T3 interfaces elongating faster. Since the results in Figure 1 above suggested that short T3 interfaces (close to the T2 configuration) elongate faster than long T3 interfaces, we wondered whether this

observed difference in progression rate between T3 and PEH interfaces could also be attributed to systematic length differences. When we examine the average lengths of T1s, T3s, and PEHs (inset in Figure 4C), we see that before the onset of GBE, T1s and PEHs start at similar lengths, as expected from the initially very regular hexagonal tissue configuration. During GBE, and during the observation time window where PEHs and T3s coexist, PEHs are much longer than newly formed T3s, as would be expected from their earlier occurrence. When we examine elongation rates specifically in the context of length (Figure 4D and Supplemental Figure S4F), we observe that the elongation rate in both T3 and PEH interfaces is indeed length dependent, and that this length-dependent rate is very similar between the two populations, with the remaining small differences possibly occurring due to sampling across time-dependent rates. These results show that, as hypothesized, the observed systematic faster elongation of T3 interfaces compared with PEHs can be attributed primarily to the systematically shorter T3 lengths. Thus these results demonstrate that horizontal elongation rates are time dependent and interface length dependent, but there is no evidence that they differ substantially between T3 interfaces and PEHs.

These results demonstrate that the cellular program for horizontal interface elongation does not differentiate between newly formed T3 interfaces and pre-existing horizontal interfaces and thus suggests that there is no molecular "privilege" that T3 interfaces gain from their history (i.e., from having been newly created through a T1 contraction event). In addition, these results show that the forces that drive horizontal extension initiate at the same time as those that drive vertical interface contraction, which suggests that AP contraction and DV elongation (convergence and extension) could conceptually be driven by a common force-generating mechanism (as opposed to two temporally and molecularly distinct processes).

Pre-existing horizontal and T3 interfaces both elongate through ratcheted steps

Given the similarity between T3 and preexisting horizontal interface rates, we wanted to know if their elongation time courses possessed similar pulsatile stepping dynamics as those that have been observed in T1 contractile events. T1 interfaces contract in a periodic manner with cycles of contraction and stabilization (Vanderleest *et al.,* 2018); we therefore investigated whether these stepping behaviors could also be seen in T3 and pre-existing horizontal interfaces. First, we employed automated step detection methods (Vanderleest *et al.,* 2018) to measure if stepped behaviors in cell area and interface lengths occur. Interestingly, we found that metrics such as step rates, durations, and step frequency were similar between T3 and pre-existing horizontal interfaces (Figure 4, E and E″; Supplemental Figure S4, C and C′).

As a second approach to examining the behaviors that lead to interface elongation, we employed our previously described approach of examining interface length changes in the context of cell area oscillations, applying the "osculating circle method" to the periodic cell area time courses (Hsu *et al.,* 2011; Vanderleest *et al.,* 2018, see *Materials and Methods*) to convert the time domain to a phase domain, which allows us to then average features (such as interface elongation rates) over multiple cell oscillation cycles even when the oscillation frequency is not constant. With this method, we found previously that T1 interface contraction occurs in a ratcheted manner during cell area oscillation cycles (Vanderleest *et al.,* 2018), with T1 interfaces contracting during the area contraction phase and stabilizing during the area expansion phase. Applying this same approach to horizontal interface elongation, we found that the same ratcheting behavior is present in both T3 and preexisting horizontal interfaces, which are stabilized at a constant length during area contraction phases and which elongate systematically during area growth phases (Figure 4F). The fastest elongation occurs at a phase angle of $\phi = 90°$, which corresponds to the time point of fastest cell area growth (see *Materials and Methods*). In summary, we find ratcheted growth in both T3 and pre-existing interfaces that mirrors the previously described T1 contraction behavior, with no significant differences between T3 and pre-existing interfaces in terms of stepping properties. This is again suggestive that elongation-driving behaviors apply equally to all horizontal interfaces, as opposed to unique elongation mechanisms associated with new T3 interfaces.

Cortical F-actin networks are required for proper T3 elongation dynamics

Branched and unbranched cortical F-actin networks are key determinants of cell and tissue topologies, and we therefore wanted to know the degree to which actin regulatory networks are implicated in the generation of elongation forces. To address this question, we generated time-lapse data sets in which either unbranched (Diaphanous) or branched (Arp2/3) actin networks were disrupted, using 50 μM SMIFH2 for Arp2/3 or 250 μM CK-666 for Diaphanous disruption, respectively. These disruptions also serve as potential perturbations of the rate metrics and dynamics described above and therefore might reveal specific aspects of these behaviors that are critical for intercalary events. The data from Diaphanous or Arp2/3 disrupted embryos demonstrated greatly reduced rates in both T1 interface contractions and T3 interface elongations relative to control embryos (Figure 5A; Supplemental Figure S5, A and A′). Interestingly, however, the time courses of the corresponding progression rates display the same symmetry between T1 and T3 behaviors as in controls, as well as the same increase in rates when interfaces are close to the T2 time point, but with an accompanying overall reduction in rates (Figure 5B). Additionally, the distributions of progression rates (measured at the –3 min time point for T1s, at 0 min for T2, and at +3 min time point for T3s) are monomodal distributions but with reduced means (Figure 5, C and C′, and Table 1). This again indicates that there is no evidence of a long-term "stalled" interface populations in any specific phase of the T1-T3 transition in F-actin disrupted embryos. Rather, we observe an across-the-board reduction of intercalary behaviors through the robust and simultaneous slowing of both T1 and T3 progression.

To further investigate the mechanism through which intercalation progress is slowed, we looked at the effect that F-actin disruption has on the pulsed steps that generate the moments of active motion that drive contractility/elongation. We found that horizontal interface elongation still occurred through ratcheted steps (Figure 5D; Supplemental Figure S5D) but that F-actin disruption strongly reduced the magnitude of ratchet steps (i.e., step "sizes") from 0.17 μm in control embryos to 0.02 μm in Dia and 0.04 μm in Arp2/3 disrupted embryos. This effect on step magnitude was seen in both T3 and pre-existing horizontal interfaces (Supplemental Figure S5, B and B′) and also in T1 contractions (Supplemental Figure S5C). We next wanted to know whether the observed reduction in ratchet step size was due to a reduction in the magnitude of the motive cell area oscillations or whether it was due to a reduced efficiency of the ratchet mechanism; in other words, a reduced ability of the cell to effectively "harness" the existing cell area oscillations to produce symmetry-breaking behaviors. To answer this question, we measured the corresponding "isotropic" interface length changes for the same dataset, that is, the changes of interface length that each cell would experience during area oscillations if the associated

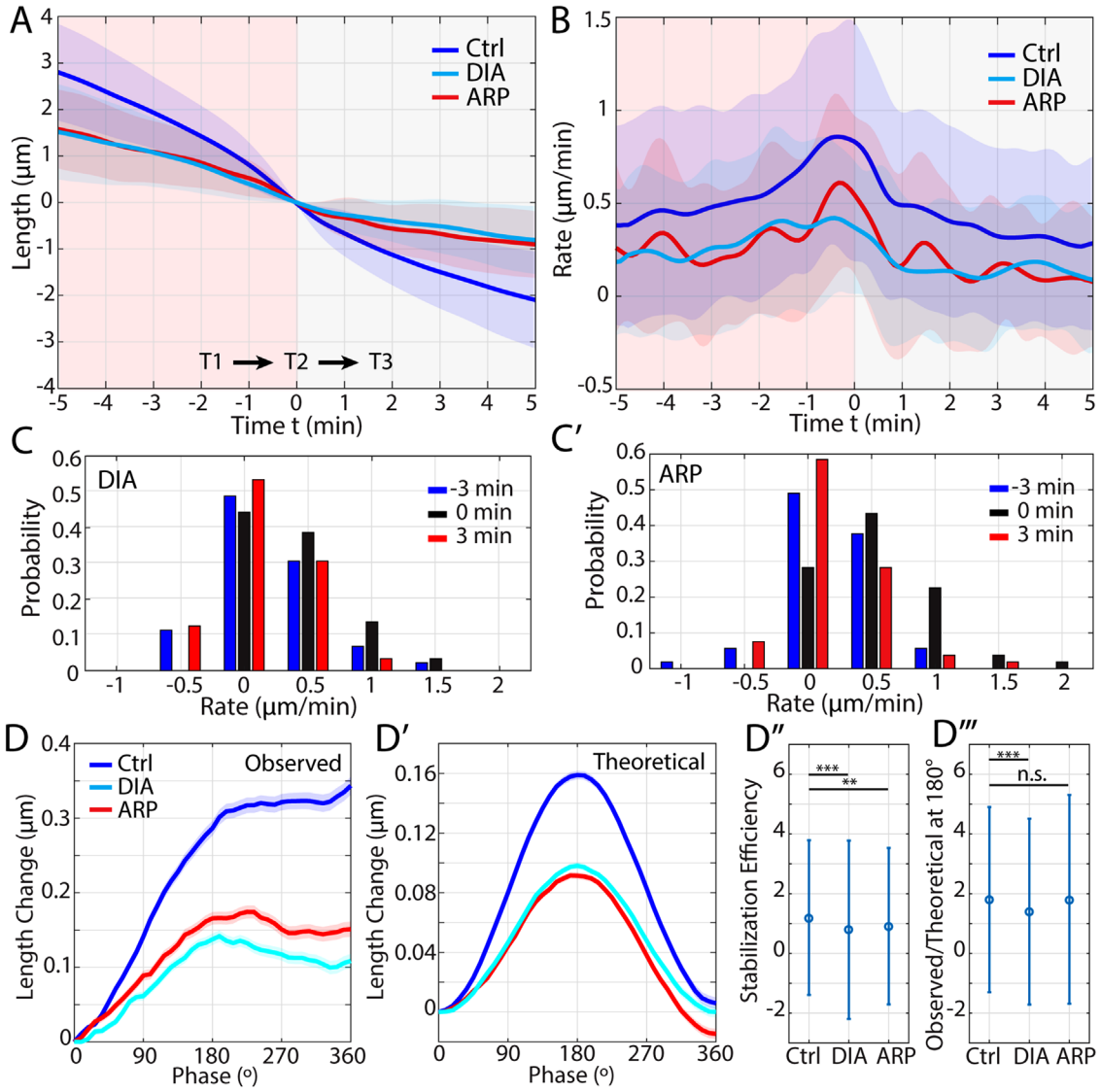

FIGURE 5: Cortical F-actin networks are required for interface elongation and high area oscillation amplitudes. (A) Mean length traces of T2-aligned transitions for Control (blue, $n = 386$ transitions, $k = 21$ embryos), Arp (red, $n = 52$, $k = 4$), and Dia (cyan, $n = 87$, $K = 4$). (B) Mean rate of contraction (during T1) and elongation (during T3) for the same transitions as in (A). Shaded confidence intervals in (A, B) represent SD. (C-C′) Distribution of rates in (B) at $t = -3$ min (in T1), $t = 0$ min (at T2), and $t = +3$ min (in T3) for Dia (C) and Arp (C′). (D) Mean length changes during cell area oscillation cycles for T3 horizontal and Pre-existing horizontal interfaces in Control (blue, $n = 4{,}659$ cycles), Dia (cyan, $n = 3603$ cycles), and Arp (red, $n = 3185$ cycles). (D′) Mean theoretical length changes during cell area oscillation cycles, assuming isotropic area oscillation for the data in (D). (D″) Ratchet stabilization efficiency of the data in (D). (D‴) Ratio of observed length change to theoretical length change at Phase angle 180°. Shaded confidence intervals in (D-D′) represent SEM. Error bars in (D″ and D‴) represent SD.

perimeter oscillations were distributed equally across all interfaces without any directional preferences. The results (Figure 5D′; Supplemental Figure S5C′) show that the predicted "isotropic" length changes are also dramatically reduced in actin-disrupted embryos, which indicates that a significant reduction of area oscillation amplitudes contributes to the defects in contraction and elongation rates. In addition to these reduced amplitudes, the ratchet was also less efficient in two different respects for Dia and Arp embryos. First, under these conditions the ratchet was less efficient at stabilizing the length during the area contraction phase (Figure 5D″), where the stabilization efficiency is measured as the ratio of the length at 360° over the length at 180°. Second, actin-disrupted cells were also less efficient than control cells at taking advantage of area oscillations overall by achieving a smaller ratchet step in proportion to the theoretical isotropic step size (Figure 5D‴). In Figure 5, D″ and D‴, error bars represent the SD of the respective ratios, which are calculated through error propagation from the numerator and denominator standard deviations (see distributions in Supplemental Figure S5E).

These results show that the F-actin network is necessary to achieve proper elongation of horizontal interfaces; specifically, they suggest that F-actin function is required to maintain robust area oscillations, and that reduced area oscillation amplitudes—even in the presence of intact symmetry-breaking mechanisms—produce smaller ratchet step sizes thus reducing intercalation efficiency. These results suggest that the driving forces behind both vertical T1

Condition (time with respect to T2 time point)	Mean ± SD (μm/min)	Number of transitions
WT (–3 min)	0.464 ± 0.536	389
WT (0 min)	0.814 ± 0.645	389
WT (3 min)	0.326 ± 0.478	389
Arp (–3 min)	0.181 ± 0.416	52
Arp (0 min)	0.546 ± 0.425	52
Arp (3 min)	0.170 ± 0.351	52
Dia (–3 min)	0.260 ± 0.470	87
Dia (0 min)	0.370 ± 0.358	87
Dia (3 min)	0.122 ± 0.366	87

TABLE 1: Instantaneous rates of interface length progression through a T1-T3 transition.

contraction and horizontal interface elongation are the radially directed forces that regulate cell area oscillations.

Medial myosin II is associated with AP interface elongation and cell area oscillations

Given the implication of a role for radially contracting forces, we wanted to examine whether medial or interfacial recruitment of myosin II, like the elongation movements, occurs systematically in the context of area oscillations. To measure medial myosin pools, we automatically generated regions of interest (ROIs) from our segmentation of interfaces and vertices (Figure 6A; Supplemental Video S6A; see *Materials and Methods*). Thus for each measurement of a horizontally elongating interface, we had accompanying measurements of the medial intensities of the four participating cells, distinguishing specifically between the AP neighboring cells on the opposite ends of the horizontal interfaces (which we will call "Cell A" and "Cell B" in the following) and the DV neighboring cells that form the horizontal interface between them (Cells C and D).

As a first step, we performed a direct cross-correlation between 1) the time trajectories of interface elongation and 2) the time trajectories of the rate of change of the corresponding Cells AB/Cells CD ratio of the medial myosin intensity. We found that this medial myosin ratio change is highly correlated to horizontal interface lengthening, and that the increase of the myosin ratio precedes T3 elongation by several seconds (red curve in Figure 6B). These results are consistent with those observed in a similar correlation analysis (Collinet *et al.*, 2015). Interestingly, however, we also see a strong correlation with an *absence* of myosin at the newly growing T3 interface (Figure 6A′; Supplemental Video S6B; cyan curve in Figure 6B). We also performed the analogous cross-correlation analysis with F-actin intensities in the same ROIs and observed qualitatively similar results to those with myosin, although magnitudes were greatly reduced (Supplemental Figure S6A). These results suggest that an asymmetric balance of tension-producing myosin II promotes interface growth, with decreased junctional myosin II at the growing interface leading to a weaker pulling tension competing against the high medial myosin present in Cells AB and with Cells CD also demonstrating a weaker medial tensile force.

Oscillation phase differences are the best predictors of AP interface elongation

We next examined whether medial myosin intensities—and by extension, the AP/DV medial myosin ratios used for the analysis above—were specifically correlated to cell area oscillations. For this purpose, we measured myosin intensities as a function of cell area oscillation phase (Figure 6C) using the same approach as for Figure 4F above, and we further differentiated between medial myosin intensities in the side regions (corresponding to the blue highlighted regions in Cells C and D in Figure 6A) and those in the top/bottom regions (corresponding to the red highlighted regions in Cell A and B in Figure 6A) of the same cell. We found that medial myosin intensities do indeed systematically correlate with cell area oscillation phase, and that medial myosin oscillations are shifted relative to area oscillations, with peak myosin intensity occurring around a cell phase of $\varphi = -45°$ (Figure 6C). The data also show that the side and the top/bottom medial myosin signals, while in phase with each other within the same cell, have slightly different amplitudes. This suggests that the medial myosin signal may still have anisotropic magnitudes in different cell regions.

Notably, since we find that the medial myosin signal is actually periodic with area oscillations, it is clear that the ratio of AP/DV medial myosin intensities (which we used for the correlation in Figure 6B above) reports on both oscillation phases and phase relationships of the participating AP and DV cells. In addition, we have already shown separately for AP and DV cells (Figure 4F and Supplemental Figure S4B) that specific phase conditions promote horizontal interface elongation; this finding also holds true when considering the simultaneous effect of the phase of AP and DV cells on elongation (Supplemental Figure S6B). Based on these findings, we wanted to determine whether the configuration of phase relationships between all four participating cells is actually sufficient to robustly predict the elongation of horizontal interfaces. To answer this question, we calculated a simple "phase alignment metric" that captures both features of the individual phases and of the phase relationships between the four cells for each time point (see *Materials and Methods*). This metric is by definition a unitless number ranging between –1 to +1. Its value is maximized when the AP neighboring cells (Cells A and B) are in phase with each other and at the phase point corresponding to maximum cell area contraction speed while simultaneously the DV neighboring cells (Cells C and D) are also in phase with each other and at the phase point corresponding to maximum area expansion speed (Figure 6D).

We find that large values of the phase alignment metric do indeed coincide with strong horizontal interface elongation and with high AP/DV myosin ratios (Figure 6D blue and red shaded regions) as expected; thus we next calculated the direct cross-correlation of this phase alignment metric with the rate of horizontal interface elongation (Figure 6B, blue line). This correlation function has a strong maximum at lag $\tau = 0$ (i.e., with no discernible time shift). Notably, the correlation magnitude here is significantly higher than the correlation magnitude of horizontal interface elongation against the medial myosin intensity ratio (compare to Figure 6B, red line). Intriguingly, this indicates that the phase (and phase differences) of the macroscopically measured area oscillations of the four participating cells are a significantly better predictor of net elongation forces on the horizontal interface than the locally measured myosin intensities (and ratios) at the vertices (also see Supplemental Figure S6C). For all three correlations shown in Figure 6B, we find a qualitatively similar result in T1 interfaces but with negative correlation magnitudes for both the phase metric and the myosin ratio (Supplemental Figure S6D). The flipping of the phase metric correlation indicates that T1 interface contraction is reliably predicted by the exact opposite phase configuration, that is, by area contraction of the two cells forming the interface and area expansion of the two cells on opposite ends of the interface—which is as expected for the

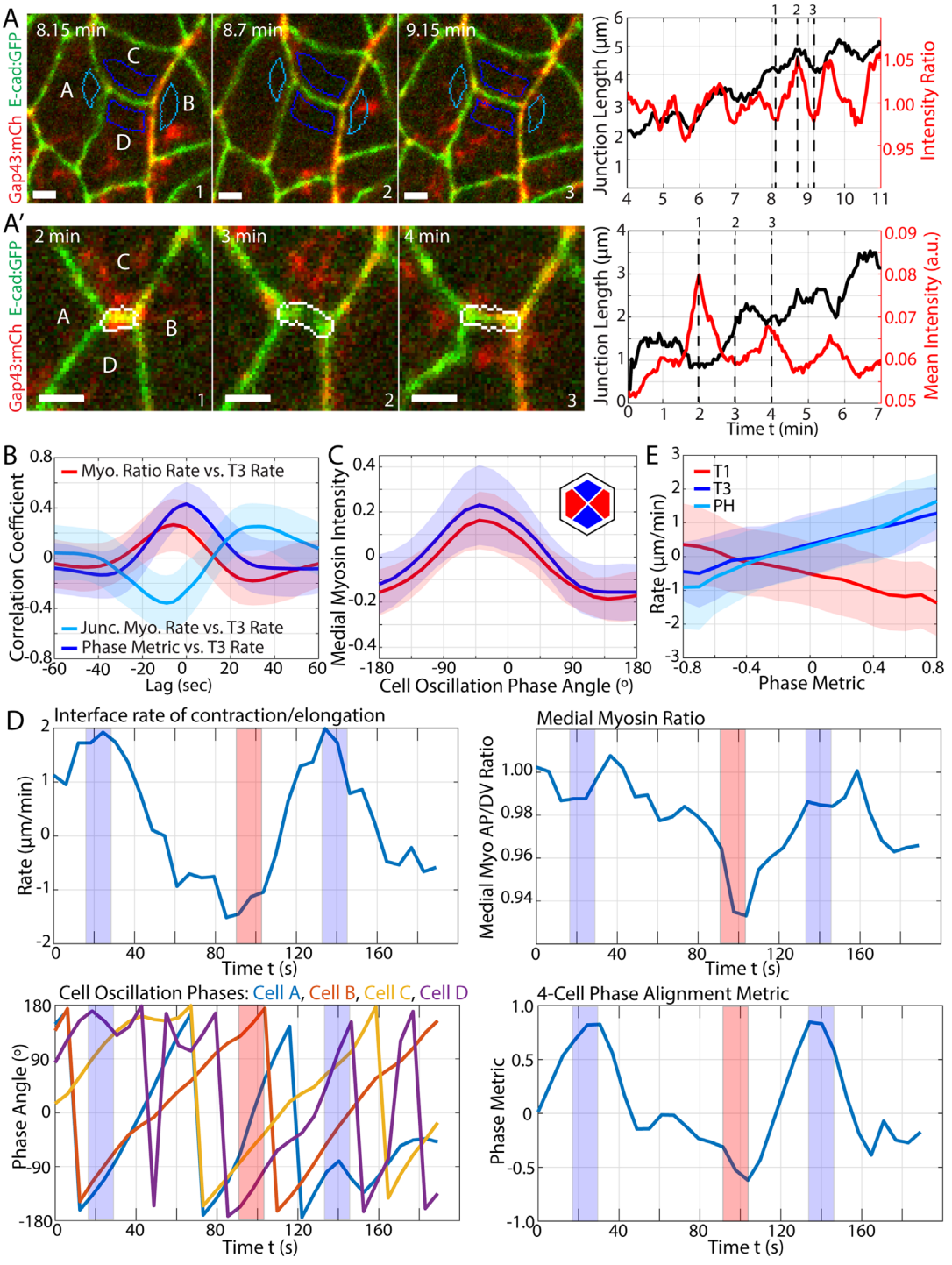

FIGURE 6: Cell oscillation phase predicts T3 interface elongation. (A) Medial myosin during T3 interface growth. The myosin intensity ratio is the intensity of the medial regions in cells A and B (cyan outlines) divided by the intensity of the medial regions in cells C and D (blue outlines). The plot at the right shows interface length (black plot line; left *y* axis) and the medial myosin ratio (red plot line; right *y* axis). The three dashed lines correspond to the 3 frames shown. (A′) Junctional myosin during T3 growth where the junctional ROI is outlined in white; the plot at the right again shows interface length and corresponding junctional myosin intensity. (B) Temporal cross-correlation of the rate of change of T3 interface length versus the rate of change of the Medial myosin Ratio (red), versus the rate of change of junctional myosin (cyan), and versus the Phase Metric (blue); $n = 98$ T3 interfaces. (C) Medial myosin as a function of cell area oscillation phase in the dorsal/ventral (blue) and anterior/posterior (red) medial regions of the cell, $n = 592$ cells. (D) Sample traces of the time course of the rate of change of a T3 length (top left), corresponding cell area oscillation phase angles of cells A, B, C, and D (bottom left), corresponding Medial myosin Ratio (top right), and corresponding Phase Metric (bottom right). (E) Interface length rate as a function of the Phase Metric for T1 interfaces (red, $n = 58$ interfaces), T3 horizontal interfaces (blue, $n = 98$ interfaces), and pre-existing horizontal interfaces (cyan, $n = 46$); each analyzed interface had a lifetime of at least 5 min. Shaded confidence intervals in B, C, and E represent SD. Scale bars are 2 μm. All data above from $k = 5$ embryos.

combined phases in T1 (Vanderleest *et al.*, 2018). But more importantly, these results show that T1 interface contraction is accompanied by a similar robust and time-shifted change of the ratio of medial myosin intensities as T3 elongation, merely inverted due to inverted phases, indicating that the role of myosin-dependent radial forces is analogous between T1 and T3 dynamics.

Subsequently, we directly calculated the rate of interface elongation as a function of the corresponding phase metric values (Figure 6E, blue curve), which shows that T3 interface elongation depends fairly linearly on the phase alignment metric, with the highest elongation occurring as expected for a phase metric of +1 and the highest contraction for –1. This linear relationship is consistent with the net motive force on each vertex being a superposition of the three radially directed forces from the three participating cells (see Supplemental Figure S6E), which are individually oscillating and thus—depending on the combination of phases within the group of cells—producing a range of intermediate forces and elongation outcomes. In addition, the curve does not go through the origin but is shifted upward where this shift (which biases the process toward T3 elongation) reflects the planar polarity of forces that drives symmetry breaking in this system. The corresponding curve looks virtually identical for pre-existing horizontal populations (Figure 6E, cyan curve), indicating again that the elongation dynamics of different types of horizontal interfaces are driven by the same force gradients. In addition, it is notable that the corresponding interpolated curve for contracting T1 interfaces looks like a perfect mirror image of the elongating interfaces (Figure 6E, red curve), where the curve is simply inverted and shifted by the same amount to bias interface dynamics toward contraction. This again suggests that the driving force dynamics for T1 contraction and T3 elongation are part of the same continuum of planar polarized forces, where the transient net motive force on each vertex is predicted robustly by the radial pulling forces of all participating cells, and where a single system of directional preference produces the symmetry breaking that biases vertex sliding movements toward intercalatory behavior—toward interface contraction in vertical and toward interface elongation in horizontal interfaces.

DISCUSSION

In our reported results, we have examined the origin of the active local T3 interface elongation forces as well as the behavioral dynamics of T1 interface contraction and T3 elongation. Time courses of T1 contraction and T3 elongation are symmetrically similar, where the speed of both contraction and elongation are faster as interfaces shorten and approach the T2 time point. Systematic wait times in the T2 state are not observable, arguing against any potential stalled subpopulations of T2s and suggesting that T1 interface contractile behaviors transition readily into T3 elongation events. Thus if the T2 state does represent a molecularly or mechanistically distinct intermediate state, then the associated transition rates are extremely fast compared with the T1 contraction and T3 elongation rates.

The striking symmetry between T1 and T3 interfaces' temporal dynamics is echoed in the sliding behavior; like T1 contractions (Vanderleest *et al.*, 2018), T3 interface elongations occur through the sliding motion of individual vertices with length compensation between T3 interfaces and neighboring transverse interfaces. In addition, our results confirm that T3 interface elongation—like T1 contraction—occurs through an active mechanism. While in computational models passive cell shape relaxation is sufficient to drive T3 elongation (Glazier and Graner, 1993; Käfer *et al.*, 2007; Rauzi *et al.*, 2008; Hilgenfeldt *et al.*, 2008; Aigouy *et al.*, 2010), experimentally observed T3 elongation in the germ band is actually associated with only minimal shape relaxation behavior, suggesting that elastic shape forces may only be sufficient to impose an upper limit to cell deformations but not to drive T3 elongations at the observed rates. This is consistent with other studies that have argued for a role of active processes in elongation (Collinet *et al.*, 2015; Yu and Fernandez-Gonzalez, 2016).

When we examined the temporal onset of T3 elongation behavior, we found some surprising results. First, we found that the planar polarized processes that produce horizontal driving forces are initialized at the same time as those processes driving T1 interface contraction, and that these drive the elongation of pre-existing horizontal interfaces long before any substantial numbers of new T3 are created. Moreover, these pre-existing interfaces display virtually identical elongation dynamics as T3 interfaces, including the relationship between length and elongation rate. Thus whatever mechanism promotes the elongation of T3 interfaces, it is not a molecularly distinct identity that carries over from the preceding T1 contraction and T2 vertex formation but a directional polarity of behavior that produces (length-dependent) elongation in all available horizontal interfaces. In addition, the pre-existing horizontal interfaces display the same ratcheting behavior as T3 interfaces. Thus we suggest that there is nothing unique about T3 interfaces (i.e., interfaces that are newly created from T1 contraction and resolution of T2 configuration) but that elongation behavior of all horizontal interfaces is a universal function of planar interface orientation. In addition, these results show that horizontal interface elongations, like T1 contractions (Vanderleest *et al.*, 2018), occur as opportunistic ratchetlike steps by harnessing the forces generated at the vertices during cell area oscillations, which are directed mostly radially toward the cell center (Lan *et al.*, 2015)

If there is a universal mechanism that drives both vertical interface contraction and horizontal interface elongation, then one of its putative regulators is F-actin. We observe that F-actin disruption significantly and symmetrically reduces both T1 interface contraction and horizontal interface elongation speed. While the time spent in the T2 configuration increases, this increase is consistent with overall lower contraction and elongation speed (and increased time spent in any length interval). Thus like in the wild-type embryos, contraction and elongation speeds of short interfaces remain slightly faster than those of longer interfaces. The primary cause of the overall reduced speed of elongation is the dramatic decrease of the amplitude of ratcheting steps (along with a smaller decrease in the ratcheting efficiency). Notably, the reduced elongation ratchet step size is associated with a strong reduction in the amplitude of the associated cell area oscillations. This is consistent with the idea that ratcheting steps directly exploit the radial forces generated during area oscillation steps and that, in F-actin disruption, decreased radial forces thus reduce the motive forces on vertices.

In addition to F-actin, we also wanted to examine the role of medial myosin II in these processes, since it had been previously proposed that transient asymmetric pulses of medial myosin II generate the required driving force for T3 elongation at AP vertices (Collinet *et al.*, 2015). Similar to the cited study, we find that medial myosin II pulses at AP vertices are associated with horizontal interface elongation. However, we also observe analogous but symmetrically inverted (with respect to the oscillation phase) medial myosin II pulses associated with T1 interface contraction. Like ratchet steps and vertex myosin II populations (Vanderleest *et al.*, 2018), these myosin pulses are periodic and occur in the context of cell area oscillations. We additionally observe that myosin II is systematically depleted from the growing T3 interface, which would be consistent with the previously

proposed reductions in T3 tensions (Yu and Fernandez-Gonzalez, 2016). Furthermore, we find that the strongest predictor for horizontal interface elongation rate is a specific combination of area oscillation phases between all participating cells, including both the AP and DV cell pair. Indeed, the correlation magnitude for the phasic driving of interface elongation is significantly higher than the magnitude observed for medial myosin II signals alone. This finding emphasizes that the experimentally measured myosin II signal is an indirect and noisy reporter of force magnitude, and it indicates that the macroscopically observable area oscillations are a robustly predictive indicator of the forces that direct interface elongation. This observed relationship between interface elongation and cell phase configuration is consistent with the net motive force on a three-way vertex being generated by a superposition of the three participating cells' radially directed forces. Again, these results are virtually identical between T3 and pre-existing horizontal interfaces and symmetrically inverted between horizontal and vertical interfaces.

Thus as opposed to two mechanically and molecularly distinct active mechanisms driving T1 contraction on the one hand and T3 elongation on the other hand, we propose that *both* T1 contraction and horizontal elongation occur conceptually through the same mechanism, which is through one main force-generating mechanism to create vertex sliding, which is combined with a system of directional bias for the stabilization of vertex sliding motions. Specifically, the radial pulling forces associated with macroscopic cell area oscillations produce transiently asymmetric forces at every vertex in the tissue, with the effective force for interface movement being the superposition of the three radial forces acting at a single vertex (see model in Supplemental Figure S6E). These three radially directed forces at every vertex are the drivers for both T1 interface contraction and horizontal elongation; they drive "agitations" of the tissue configuration that allow the tissue to explore the energy landscape and which can be exploited by the ratchet mechanism. The fact that both contraction and elongation proceed measurably faster in very short interfaces may be related to more favorable force geometries in these cases.

While this proposed mechanism does not exclude the existence of some asymmetric tension forces (e.g., in interfaces) that could bias force direction, it also does not require them: Even if the oscillating radial forces at each vertex were net isotropic—with equal net force amplitudes into the participating radial directions—the systematic preference for intercalation movements could still be sustained entirely through the anisotropic stabilization mechanisms that underly the ratchet. Thus it is conceivable that the symmetry breaking of the system could be built primarily on planar polarized mechanisms that bias vertex sliding through stabilization (e.g., through adhesion and/or membrane trafficking-dependent mechanisms; Levayer *et al*., 2011; Clément *et al*., 2017; Jewett *et al*., 2017; Miao *et al*., 2019, 2021) in the presence of net isotropic forces as opposed to a priori generating strongly anisotropic forces to orient vertex sliding direction.

MATERIALS AND METHODS

Fly stocks and genetics

Stocks were kept at 25°C and maintained by standard procedures. Fly stocks used in this study were Resille:GFP; Spider:GFP (cell outline markers) and Gap43:mCh (a cell outline marker), moeABD:GFP (a F-Actin reporter), and E-cad:GFP (a marker of cell junctions); mCherry:Sqh (Sqh is the myosin regulatory light chain of nonmuscle myosin II in *Drosophila*). E-cad:GFP was expressed from the endogenous locus of E-cadherin on the second chromosome and is homozygous viable.

Live imaging

Embryos were collected on apple juice agar and dechorionated in 50% bleach for 2 min, then rinsed with water and either staged on apple juice agar or transferred to a gas-permeable microscope slide and covered with Halocarbon 27 oil. All imaging was performed on a CSU10b Yokogawa spinning disk confocal from Zeiss and Solamere Technologies Group with a 63×/1.4 NA objective, with the exception of myosin II movies, which were obtained on a CSUX1FW Yokogawa spinning disk confocal from Nikon and Solamere Technologies Group with a 60×/1.4 NA objective. Ecad:GFP; mCh:sqh images are a maximum intensity projection of 5–10 z-slices taken at 0.75-μm steps at ~6 s/frame.

Drug injections

Following dechorionation as previously described, embryos were staged and aligned on apple juice agar, glued to a coverslip with heptane glue and desiccated. Embryos were covered with Halocarbon 700 oil then injected with 250 μM CK-666 (an Arp2/3 inhibitor, TOCRIS cat #3950) or 50 μM SMIFH2 (a Dia/Formin inhibitor, TOCRIS cat #4401). Embryos at early GBE were injected in the perivitelline space at 50% egg length.

Repeatability

All measurements were quantified from a minimum of three embryos and represented at least two individual trials.

Cell segmentation

Image and data analysis were performed in MATLAB (MathWorks). Cells were segmented using a seeded watershed algorithm and tracked in time. Cell areas were measured as the sum of the pixels within the contour of the watershed segmentation lines.

Interface lengths

Interface lengths were measured as the Euclidean distance between vertices, where vertices are the positions where three or more cells meet. Due to the pixelated nature of the watershed transform, interface lengths are measured with a precision of single pixels, and noisy variations in length are present due to confocal imaging and its interpretation by the watershed algorithm. Another consequence is that very short interfaces (1–2 pixels long, corresponding to <0.5 microns) are difficult to distinguish from higher-order vertices (such as T2 or rosette configurations). To address this issue, in some of our analysis we applied a Gaussian filter to the raw length traces to better approximate "true" interface lengths (green trace in Figure 1A′).

T2 alignment time

To find the T2 time point of a transition, we combine the T1 length trace and the T3 length trace into a single length trace where T1 length is assigned a positive sign and T3 length a negative sign, so that progression is in the same direction of decreasing length (Figure 1A′). We Gaussian-filtered the full-length trace with a sigma of 40 s (green trace in Figure 1A′). The T2 time point is the first time point at which the filtered trace is less than or equal zero (dashed black line in Figure 1A′).

T2 aligned rate

The rate of length change for type T1 transitions was found using a centered difference formula, $r(t) = [L(t + \Delta t/2) - L(t - \Delta t/2)]/\Delta t$, where $\Delta t = 30$ s, and where we took the rate of the Gaussian-filtered (sigma = 40 s) length trace. The centered difference was used to avoid a temporal bias.

Dwell times in T1, T2, and T3

A challenge in measuring the dwell time spent in T2 is that the watershed-based segmentation is not very accurate in distinguishing between very short interfaces and T2 configurations. Due to pixelation, there are far fewer possible configurations in which you can have a four-cell vertex (T2 state) than you can have two closely spaced three-cell vertices. Thus instead of measuring the time spent in our detected T2 state, we measured the time spent in a length range centered at the T2 time point (between equal lengths in T1 and T3) and compared that with the time spent in equal length ranges centered at T1 and T3 lengths. Dwell times were measured as the total time spent in the following five equal length bins: a long T1 length bin for 4 μm > $L \geq 2.4$ μm, a short T1 length bin for 2.4 μm > $L \geq 0.8$ μm, a T2 length bin for 0.8 $\mu m > L \geq -0.8$ μm, a short T3 length bin for –0.8 μm > $L \geq 2.4$ μm, and a long T3 length bin for –2.4 μm > $L \geq -4$ μm, where L is the Gaussian-filtered length trace (sigma = 40 s). In order for a T1 transition to be included in the Dwell Time measurements it had to be present at least 5 min before and 5 min after the T2 time point and had to exceed at least 3 microns in both T1 and T3 length. Due to this minimum length requirement, the number of T1 transitions used in Figure 1D was reduced compared with Figure 1, B and C.

Cross-correlation of T3 with transverse junctions

To measure vertex sliding on short timescales we performed a temporal cross-correlation of the T3 junction rate of change with each transverse junction rate of change. Each length trace was Gaussian-filtered (sigma = 10 s) before taking the rate. Rates were calculated over a time interval of 30 s, and an unbiased cross-correlation was performed on each pair of junctions that existed for at least 5 min. Each T3 junction was cross-correlated with each of its four transverse junctions.

SF

The cell SF metric is defined as $P^2/4\pi A$, where P P is the cell perimeter and A is the area. Based on this definition the SF has a minimum value at 1 for perfect circles and increases as shapes become more irregular.

Pre-existing horizontal and current horizontal definitions

Pre-existing horizontal interfaces are defined as interfaces that are present from before GBE begins and have horizontal angles (>75°). However, since interfaces can change their angles over time (and even cross over our horizontal angle threshold of 75°), we used for this category only the (non-T3) horizontal interfaces during the time interval where they did in fact have angles >75° (e.g., in Figure 4, C and D). Given this definition, the sample set can slightly change over time. In contrast, our definitions of T1 and T3 interfaces are not a priori constrained by angle; they are identified by the algorithm only by virtue of being either the disappearing (T1) or the newly appearing (T3) interface of a topological transition event. However, due to the planar polarity of the biological system, T1 and T3 interfaces also naturally fall within a very narrow range of orientation angles. Distributions for the spatial orientation angles of T1 and T3 interfaces are shown in Supplemental Figure S4D.

Step detection

To detect active motion steps in our vertex position trajectories we used a rolling analysis window technique adapted from Huet *et al.* (2006; see Supplemental Figure S4, C and C′ for examples). The MSD is the customary method to classify a subtrajectory into active, diffusive, or constrained motions based on whether the MSD curves upward, is linear, or curves downward, respectively. For periods of active motion the MSD behaves as a power law $MSD(\tau) \propto \tau^{\gamma}$, where $\gamma > 1$. By calculating the parameter gamma along a trajectory using a rolling window we can identify periods of active and nonactive (i.e., either diffusive or constrained) motion. We chose a sliding window size of 57 s (N = 19 frames) because it resulted in detected steps that agreed with manually. For each time window, we fit the MSD to lags between 4 and (N-1)/2 frames where N is the odd-numbered number of points in the window. The first three lags were left out of the fitting because localization error leads to artifactual subdiffusion at this short time scale lowering the value of γ. To reduce computation time, we performed linear fitting of the MSD verses τ on a log-log plot. The determination of systematic from nonsystematic periods is made by setting a threshold on $\gamma(t)$ of 1. We applied a minimum duration requirement of 20 s because we found that positive detections below that duration didn't represent real active periods.

Phase analysis of cell area oscillations

Instantaneous cell oscillation phase is acquired from cell area oscillations using the osculating circle method (Hsu *et al.*, 2011). A more detailed explanation of the processing to acquire the cell phase can be found in Vanderleest *et al.* (2018). In our implementation, the phase angles are related to the area oscillation time courses as a $A(\varphi) = b - c \cdot \cos(\varphi)$, that is, a negative cos function. This means conceptually that a phase angle of φ = 180° corresponds to the time point of the area maximum, and that φ = 0° and φ = 360° correspond to the area minimum (Supplemental Figure S4A); therefore the phase point corresponding to the fastest rate of contraction (area decrease) is φ = –90° and the fastest rate of expansion (area increase) at φ = +90°.

For the ratchet analysis (Figures 4F and 5D), length changes ΔL were measured as the change relative to the start of the cycle at φ = 0°; thus by definition, lengths start at zero for φ = 0°. In some cases, there were oscillations detected by the osculating circle method that had extremely short durations that didn't represent area oscillations, so that we restricted our analysis to oscillations which had a minimum duration of 30 s.

Phase alignment metric

We calculated a "phase alignment metric" that captures how favorable or unfavorable the phase configuration of the participating four cells (cells A, B, C, and D) is for the elongation of a horizontal interface. Based on the findings in Figure 4F and Supplemental Figure S6B (showing that elongation is maximized for a phase angle of φ = –90° in the AP neighboring cells A and B and for a phase angle φ = +90° in the DV neighboring cells C and D), this phase alignment metric was defined as

$$metric = \frac{1}{4} \cdot [\cos(\varphi_C - 90°) + \cos(\varphi_D - 90°) + \cos(\varphi_A + 90°) + \cos(\varphi_B + 90°)]$$

where φ_A, φ_B, φ_C, and φ_D, are the oscillation phase angles of cells A, B, C, and D. This metric is by definition a unitless number ranging between –1 and +1. The choice of offsets in the equation determines that the value of the metric is automatically maximized at those time points when cells A and B are both at phase angle φ = –90°, that is, when they are contracting at the fastest rate (as discussed above in the section on the phase analysis) and when cells C and D are at phase angle φ = –90°, when they are expanding at the fastest rate.

Myosin intensity ROIs

ROIs for both medial and junctional intensity measurements were automatically generated from the tissue segmentation results for each time point. The junctional ROI was generated by computing the distance transform of the cell–cell junction and taking all pixels within a distance of 4 pixels (~0.6 microns). Medial ROIs were also generated using a distance transform of the junction. The medial ROIs for cells C and D (see Figure 6A) were taken to be between 5 and 18 pixels (~0.7 to 2.5 microns) from the T3 junction and at least 5 pixels from all neighboring junctions. The Medial ROIs for cells A and B were taken to be between 5 and 18 pixels from the T3 vertex and at least 5 pixels from the neighboring junctions. Measurements of the ROI average intensity were done on maximum projections of between 6 and 10 apical z-layers.

Statistics

For all box-and-whisker plots (MATLAB statistics toolbox box plot), the central mark indicates the median, and the bottom and top edges represent the 25th and 75th percentiles, respectively. The whiskers represent the extreme values not including outliers, where outliers are defined as being more than 1.5 times the interquartile range from the bottom or top of the box.

ACKNOWLEDGMENTS

We thank the Blankenship and Loerke labs for discussions and critical reading of the manuscript. This work was supported by National Institutes of Health (NIH) Grant R15 GM126422 to J.T.B., NIH Grant R15 GM117463 to D.L., and NIH Grant R01 GM127447 to J.T.B. and D.L.

REFERENCES

Aigouy B, Farhadifar R, Staple DB, Sagner A, Röper J-C, Jülicher F, Eaton S (2010). Cell flow reorients the axis of planar polarity in the wing epithelium of Drosophila. Cell 142, 773–786.

Bardet P-L, Guirao B, Paoletti C, Serman F, Léopold V, Bosveld F, Goya Y, Mirouse V, Graner F, Bellaïche Y (2013). PTEN controls junction lengthening and stability during cell rearrangement in epithelial tissue. Dev Cell 25, 534–546.

Bertet C, Sulak L, Lecuit T (2004). Myosin-dependent junction remodelling controls planar cell intercalation and axis elongation. Nature 429, 667–671.

Blankenship JT, Backovic ST, Sanny JSP, Weitz O, Zallen JA (2006). Multicellular rosette formation links planar cell polarity to tissue morphogenesis. Dev Cell 11, 459–470.

Clément R, Dehapiot B, Collinet C, Lecuit T, Lenne P-F (2017). Viscoelastic Dissipation Stabilizes Cell Shape Changes during Tissue Morphogenesis. Curr Biol CB 27, 3132–3142.e4.

Collinet C, Rauzi M, Lenne P-F, Lecuit T (2015). Local and tissue-scale forces drive oriented junction growth during tissue extension. Nat Cell Biol 17, 1247–1258.

Farhadifar R, Röper J-C, Aigouy B, Eaton S, Jülicher F (2007). The influence of cell mechanics, cell-cell interactions, and proliferation on epithelial packing. Curr Biol CB 17, 2095–2104.

Fernandez-Gonzalez R, Simoes de SM, Röper J-C, Eaton S, Zallen JA (2009). Myosin II dynamics are regulated by tension in intercalating cells. Dev Cell 17, 736–743.

Garcia De Las Bayonas A, Philippe J-M, Lellouch AC, Lecuit T (2019). Distinct RhoGEFs activate apical and junctional contractility under control of G proteins during epithelial morphogenesis. Curr Biol CB 29, 3370–3385.e7.

Glazier JA, Graner F (1993). Simulation of the differential adhesion driven rearrangement of biological cells. Phys Rev E Stat Phys Plasmas Fluids Relat Interdiscip Topics 47, 2128–2154.

Guillot C, Lecuit T (2013). Mechanics of epithelial tissue homeostasis and morphogenesis. Science 340, 1185–1189.

Hilgenfeldt S, Erisken S, Carthew RW (2008). Physical modeling of cell geometric order in an epithelial tissue. Proc Natl Acad Sci USA 105, 907–911.

Hsu M-K, Sheu J-C, Hsue C (2011). Overcoming the negative frequencies - Instantaneous frequency and amplitude estimation using Osculating Circle method. J Mar Sci Technol 19, 514–521.

Huet S, Karatekin E, Tran VS, Fanget I, Cribier S, Henry J-P (2006). Analysis of transient behavior in complex trajectories: application to secretory vesicle dynamics. Biophys J 91, 3542–3559.

Irvine KD, Wieschaus E (1994). Cell intercalation during Drosophila germband extension and its regulation by pair-rule segmentation genes. Dev Camb Engl 120, 827–841.

Jewett CE, Vanderleest TE, Miao H, Xie Y, Madhu R, Loerke D, Blankenship JT (2017). Planar polarized Rab35 functions as an oscillatory ratchet during cell intercalation in the Drosophila epithelium. Nat Commun 8, 476.

Käfer J, Hayashi T, Marée AFM, Carthew RW, Graner F (2007). Cell adhesion and cortex contractility determine cell patterning in the Drosophila retina. Proc Natl Acad Sci USA 104, 18549–18554.

Keller R, Davidson L, Edlund A, Elul T, Ezin M, Shook D, Skoglund P (2000). Mechanisms of convergence and extension by cell intercalation. Philos Trans R Soc Lond B Biol Sci 355, 897–922.

Keller R (2002). Shaping the vertebrate body plan by polarized embryonic cell movements. Science 298, 1950–1954.

Lan H, Wang Q, Fernandez-Gonzalez R, Feng JJ (2015). A biomechanical model for cell polarization and intercalation during Drosophila germband extension. Phys Biol 12, 056011.

Lau K, Tao H, Liu H, Wen J, Sturgeon K, Sorfazlian N, Lazic S, Burrows JT, Wong MD, Li D, *et al.* (2015). Anisotropic stress orients remodelling of mammalian limb bud ectoderm 17, 569–579.

Levayer R, Pelissier-Monier A, Lecuit T (2011). Spatial regulation of Dia and Myosin-II by RhoGEF2 controls initiation of E-cadherin endocytosis during epithelial morphogenesis. Nat Cell Biol 13, 529–540.

Levayer R, Lecuit T (2013). Oscillation and polarity of E-cadherin asymmetries control actomyosin flow patterns during morphogenesis. Dev Cell 26, 162–175.

Loerke D, Blankenship JT (2020). Viscoelastic voyages - Biophysical perspectives on cell intercalation during Drosophila gastrulation. Semin Cell Dev Biol 100, 212–222.

Miao H, Vanderleest TE, Jewett CE, Loerke D, Blankenship JT (2019). Cell ratcheting through the Sbf RabGEF directs force balancing and stepped apical constriction. J Cell Biol 218, 3845–3860.

Miao H, Vanderleest TE, Budhathoki R, Loerke D, Blankenship JT (2021). A PtdIns(3,4,5)P_3 dispersal switch engages cell ratcheting at specific cell surfaces. Dev Cell 56, 2579–2591.e4.

Munjal A, Philippe J-M, Munro E, Lecuit T (2015). A self-organized biomechanical network drives shape changes during tissue morphogenesis. Nature 524, 351–355.

Nikolaidou KK, Barrett K (2005). Getting to know your neighbours; a new mechanism for cell intercalation. Trends Genet TIG 21, 70–73.

Rauzi M, Verant P, Lecuit T, Lenne P-F (2008). Nature and anisotropy of cortical forces orienting Drosophila tissue morphogenesis. Nat Cell Biol 10, 1401–1410.

Sawyer JK, Choi W, Jung K-C, He L, Harris NJ, Peifer M (2011). A contractile actomyosin network linked to adherens junctions by Canoe/afadin helps drive convergent extension. Mol Biol Cell 22, 2491–2508.

Simões de SM, Blankenship JT, Weitz O, Farrell DL, Tamada M, Fernandez-Gonzalez R, Zallen JA (2010). Rho-kinase directs Bazooka/Par-3 planar polarity during Drosophila axis elongation. Dev Cell 19, 377–388.

Simões de SM, Mainieri A, Zallen JA (2014). Rho GTPase and Shroom direct planar polarized actomyosin contractility during convergent extension. J Cell Biol 204, 575–589.

Solnica-Krezel L (2005). Conserved patterns of cell movements during vertebrate gastrulation. Curr Biol CB 15, R213–R228.

Vanderleest TE, Smits CM, Xie Y, Jewett CE, Blankenship JT, Loerke D (2018). Vertex sliding drives intercalation by radial coupling of adhesion and actomyosin networks during Drosophila germband extension. eLife 7.

Wallingford JB, Fraser SE, Harland RM (2002). Convergent extension: the molecular control of polarized cell movement during embryonic development. Dev Cell 2, 695–706.

Yu JC, Fernandez-Gonzalez R (2016). Local mechanical forces promote polarized junctional assembly and axis elongation in Drosophila. eLife 5, e10757.

Zallen JA, Wieschaus E (2004). Patterned gene expression directs bipolar planar polarity in Drosophila. Dev Cell 6, 343–355.